University of Nottingham

School of Mathematical Sciences

The Effects of Network Topology on Renewable-Integrated Microgrid Stability

---

Authors:

Jiatong Jin, Huanyang Tan, Xiaoyi Jiang,
Matthew Jackson, Katherine Cornwall, Emily Earl

Module Lecturers:

Professor Jonathan Wattis & Professor Etienne Farcot

MATH3060 - Applied Mathematical Modelling

Last Updated: March 2, 2026

Abstract

Abstract to be written. This will summarise the causal chain from model development through problem identification, topology intervention, and the stability–resilience paradox.

Contents

1   Introduction

Renewable generation is reshaping electricity systems at an unprecedented pace. The International Energy Agency projects that renewables will account for the majority of new capacity installed globally within this decade [1], and in the United Kingdom alone, they supplied over 50% of total electricity in 2024 [4]. A large share of this growth comes from distributed photovoltaic (PV) installations at household and community scale, which are transforming how electricity networks are structured. Classical grids depend on a handful of large, centralised generators feeding high-voltage transmission lines; microgrids, in contrast, draw on many small, intermittent sources spread across the low-voltage distribution layer [6]. Managing synchronisation and stability in such systems requires tools that conventional grid-planning methods were not designed to provide.

Coupled-oscillator models derived from the swing equation are the standard theoretical lens for power-network stability. Filatrella et al. [7] showed that the second-order Kuramoto model captures the interplay between power injection, damping, and sinusoidal coupling with enough physical fidelity to be analytically tractable. Rohden et al. [11] took this further, demonstrating that self-organised synchronisation can emerge in decentralised grids without central frequency control, though the outcome is sensitive to network topology. Nishikawa and Motter [10] compared several synchronisation formulations and identified the conditions under which they produce equivalent stability predictions. The most comprehensive treatment of the problem—covering the Jacobian structure, the implicit function theorem, and saddle-node bifurcation at the stability boundary—was provided by Dörfler and Bullo [5]. Together, these works supply the analytical foundation on which the present study builds.

Synchronisation failure is not the only path to grid collapse. Cascading overload presents an equally serious threat and operates through entirely different dynamics. Watts [17] established a general threshold model showing how a localised perturbation on a random network can escalate into a system-wide failure. Carreras et al. [2] brought this framework to power transmission, identifying critical operating points where the system tips from resilient to vulnerable. Motter and Lai [9] found that targeted removal of high-load nodes triggers cascades out of proportion to the initial disturbance, pointing to network heterogeneity as a key amplifier. Schäfer et al. [12] showed more recently that cascade dynamics can be induced purely by internal power-flow redistribution following a single line trip, without any external shock. Manik et al. [8] extended the picture further, demonstrating that certain topological configurations create localised stress concentrations capable of destabilising an otherwise healthy system.

These stability concerns have driven sustained interest in topology optimisation as a design lever. Witthaut and Timme [19] showed that a single added transmission line can paradoxically destroy synchronisation in an oscillator network—a power-grid instance of the classical Braess paradox—cautioning that well-intentioned upgrades can backfire. Coletta and Jacquod [3] analysed the same phenomenon through linear stability theory, characterising the conditions under which edge additions help or hurt. On the constructive side, Skardal et al. [13] developed a rewiring algorithm for inertial Kuramoto networks that substantially lowers synchronisation thresholds through targeted restructuring. Zhang et al. [20] examined how heterogeneous edge placements affect synchronizability, finding that the benefit or cost of an added edge depends non-trivially on both its location and the number of edges already present.

What most of this literature shares, however, is a reliance on synthetic or idealised power distributions. Real microgrids operate under household demand and PV generation profiles that

shift continuously across diurnal and seasonal cycles, producing time-varying nodal power injections that repeatedly reconfigure the network's operating state. These temporal fluctuations give rise to failure modes and structural bottlenecks that simply do not appear in static or uniformly distributed models.

The present study bridges this gap by coupling the swing-equation framework of Smith et al. [14] with measured smart-meter consumption data from London households [16] and photovoltaic generation records from UK Power Networks [15], all embedded in Watts–Strogatz small-world topologies [18]. Rather than generic network disorder, this data-driven approach points to a specific structural bottleneck at the point of common coupling (PCC), where the entire microgrid's aggregate surplus must pass through a small number of edges. The investigation unfolds in four stages: locating the PCC bottleneck from temporal dynamics, developing and analytically justifying a targeted degree-augmentation intervention, evaluating it against both synchronisation and cascade failure modes, and testing its robustness across damping regimes representing different levels of renewable penetration.

The report is structured as follows. Section 2 develops the mathematical model and traces the PCC bottleneck through progressively realistic scenarios. Section 3 establishes the analytical basis for the topology intervention and compares edge-addition strategies. Section 4 presents systematic experiments covering budget scaling, cascade failure, and damping sensitivity. Section 5 draws these threads together, interprets the stability–resilience paradox, and identifies directions for future work.

2   Mathematical Model & Problem Identification

This chapter develops the mathematical framework used throughout the report and applies it to progressively more realistic scenarios. Beginning from the swing equation and its baseline verification, the analysis moves through static power distribution effects to time-dependent data-driven dynamics, culminating in the identification of a structural bottleneck that motivates the topology intervention of section 3.

2.1   Swing Equation Framework

To model network dynamics and conduct analysis, we will use the second-order swing equation:

$$\frac{d^2\theta_k}{dt^2} + \gamma \frac{d\theta_k}{dt} = P_k - \kappa \sum_{l=1}^{n} A_{kl} \sin(\theta_k - \theta_l), \quad k = 1, 2, \ldots, n. \tag{1}$$

This portrays power grids as a connected network of n rotating machines (regarded as nodes), with phase angle $\theta_k(t)$. P_k denotes the power generation (positive) and consumption (negative) of the kth node, γ is a uniform damping coefficient that models dissipative effects, κ is the global coupling strength that represents the strength of power transmission through the grid, and A_{kl} is the network adjacency matrix. The power flow along each edge (k, l) is determined by

$$f_{kl} = \kappa \sin(\theta_k - \theta_l). \tag{2}$$

In the UK every node must remain synchronised to 50Hz (ref?), synchronisation is interpreted as frequency locking; akk nodal frequencies converge to zero within a numerical tolerance over

a terminal time window. De-synchronisation can lead to instability, infrastructure damage, or large-scale failure of the grid. For a given network and power configuration, critical coupling (κ_c) is the smallest coupling strength that sustains synchronisation. It is estimated by bisection over κ : Eq. (1) is integrated from randomised initial conditions, convergence is checked over a terminal time window, the smallest value of κ is recorded, and ensemble averages are computed for multiple network realisations.

The network composition is tracked on the configuration simplex (η_+, η_-, η_p), where

$$\eta_+ = \frac{n_+}{n}, \quad \eta_- = \frac{n_-}{n}, \quad \eta_p = \frac{n_p}{n}, \quad \text{subject to} \quad \eta_+ + \eta_- + \eta_p = 1, \tag{3}$$

and the class fractions are determined by the power distribution:

$$\eta_+ = \int_\epsilon^\infty \rho(P)\, dP, \quad \eta_- = \int_{-\infty}^{-\epsilon} \rho(P)\, dP, \quad \eta_p = \int_{-\epsilon}^{\epsilon} \rho(P)\, dP. \tag{4}$$

This framework, introduced by Smith et al. [14], provides a geometric interpretation of synchronisation stability: different positions on the simplex correspond to different proportions of generators, consumers, and near-zero (prosumer) nodes, with the critical coupling varying systematically across the landscape.

Unless otherwise stated, simulations use Watts–Strogatz small-world networks [18] with the parameters listed in table 1.

Table 1: Fixed simulation parameters used across all experiments, following Smith et al. [14]. Total power is normalised to unity.

Parameter	Symbol	Value
Network size	n	50
Mean degree	$\bar{K}$	4
Rewiring probability	q	0.1
Damping coefficient	γ	1
Total power	$P_{\max}$	1

2.2   Model Assumptions

The following assumptions underpin the analysis:

(i) **Homogeneous coupling** - All edges share a constant coupling strength κ; heterogeneous line impedances are not modelled.

(ii) **Uniform damping** - All nodes share a constant damping coefficient γ.

(iii) **Power balance** - The system satisfies $\sum_{k=1}^{n} P_k = 0$ at all times, enforced by symmetric class splits or by a point-of-common-coupling (PCC) slack node.

(iv) **Static topology** - The adjacency matrix A_{kl} is fixed during each simulation; no self-healing or adaptive reconfiguration is modelled.

Table 2: Key symbols used throughout the report.

Symbol	Description
κ	Coupling strength
κ_c	Critical coupling strength for synchronisation
$\hat{\kappa}_c$	Normalised critical coupling, $\kappa_c/P_{\max}$
$\bar{\kappa}_c$	Ensemble-averaged critical coupling
P_i	Net power injection at node i (positive: generator, negative: consumer)
η_+, η_-, η_p	Generator, consumer, and prosumer fractions on the configuration simplex
d_0	Baseline degree of the PCC node
m	Number of edges added by the topology intervention
S	Cascade survival ratio (fraction of edges surviving cascade)

(v) **Frequency-lock criterion** - Synchronisation occurs when $|\dot{\theta}_k(t)| < \varepsilon$ for all nodes over a terminal window.

(vi) **Small-world proxy** - Watts–Strogatz networks $WS(n = 50, \bar{K} = 4, q = 0.1)$ serve as micro-grid topology proxies.

These assumptions allow controlled comparison across the following work. Subsequent sections relax selected assumptions: section 2.5 introduces time-dependent power injections from measured data, and section 3 modifies the network topology through targeted edge additions.

2.3 Baseline Verification

Before extending the model, the numerical simulations were validated against the results of Smith et al. [14] (specifically their Figures 1C-D). In particular, the critical coupling landscape was computed over the configuration simplex for representative network realisations at rewiring probabilities $q = 0$ and $q = 0.1$. We also computed the dependence of $\bar{\kappa}_c/P_{\max}$ on the number of consumers n_- was evaluated for $q \in \{0.0, 0.1, 0.4, 1.0\}$.

This data matches the reported structure and confirms that $\bar{\kappa}_c$ is minimised when generators and consumers are balanced at the simplex centre. It also establishes that increased topological randomness q lowers the synchronisation threshold. This validation provides confidence that the numerical implementation for all subsequent work.

2.4 Static Power Distribution Effects

The verification work established the qualitative dependence of κ_c on the composition and topology of the network. A natural follow-up question is whether the distribution of power magnitudes within a fixed composition also matters. In the real-world, micro-grids have heterogeneous household demands and generation capacity is unevenly distributed. Hence, we now determine whether static heterogeneity alone can produce significant stability variations.
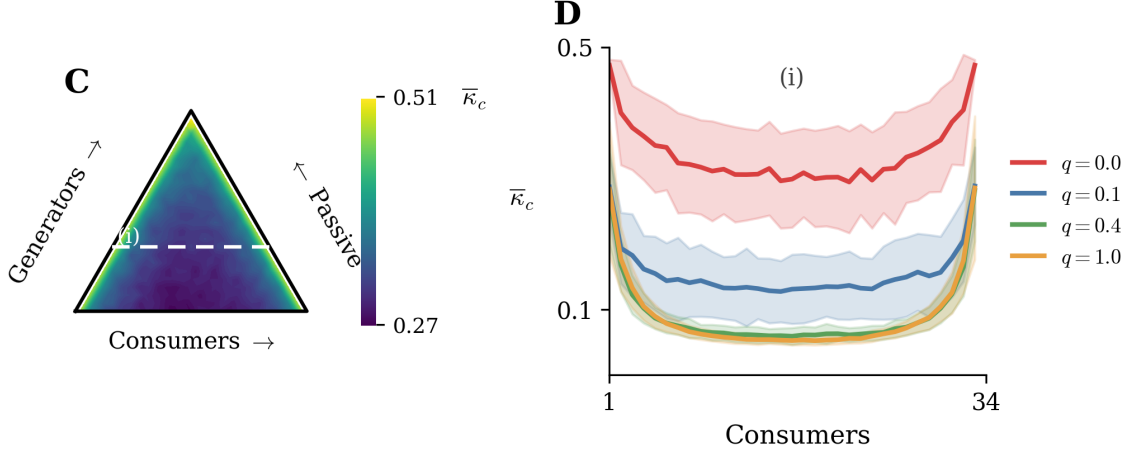
Figure 1: Reproduction of Smith et al. [14], Figures 1C–D. Left: normalised critical coupling $\bar{\kappa}_c/P_{\max}$ over the generator–consumer–prosumer composition simplex at $q = 0$ and $q = 0.1$. Right: $\bar{\kappa}_c/P_{\max}$ as a function of n_- for four rewiring probabilities. The critical coupling is minimised when generators and consumers are balanced (simplex centre) and decreases with increasing topological randomness, consistent with the published results.

To test this, two experiments were conducted on $WS(n = 50, \bar{K} = 4, q = 0.1)$ networks with fixed class counts $n_+ = n_- = 25$, total power $P_{\max} = 1.0$, and mean magnitude $\bar{P} = 0.04$. In the first, generator magnitudes were drawn from a truncated normal distribution $\mathcal{N}(\bar{P}, \sigma^2)$ and then re- normalised to preserve total generation. In the second, the same procedure was applied to consumers, preserving net power balance. The relative dispersion $\sigma/\bar{P}$ was swept over the range $[0, 0.8]$ with 200 realisations per point.

As fig. 2 shows, κ_c variation is small, about 4% across the full dispersion range (from 0.121 to 0.126), and the generator-side and consumer-side curves are statistically indistinguishable. However, this negative result is informative: it indicates that magnitude dispersion within balanced classes has negligible effect on synchronisation thresholds.

However, heterogeneity can take a different form. Rather than dispersing magnitudes symmetrically, generation may be concentrated into a small number of high-capacity nodes. To isolate this effect, a single "big station" generator was assigned a fraction, r, of total generation, while 24 small stations shared the remainder $1 - r$, with r swept over $[0.04, 0.95]$.

The contrast with the heterogeneity sweep is significant. As shown in fig. 3, κ_c increases monotonically with r, rising from 0.121 at $r = 0.04$ (uniform distribution) to 0.289 at $r = 0.95$, a 139% increase. This result suggests that concentration of generation onto a single node, rather than symmetric dispersion, is the dominant static risk factor for synchronisation stability.

Together, these results established that the shape of the power distribution within balanced classes has a limited effect on κ_c, whereas concentrating generation onto a small number of nodes gives a substantial increase. However, these are idealised, time-independent distributions. If static heterogeneity alone cannot generate large swings in synchronisation requirements, then the pronounced instability observed in real micro-grids must arise from either structural concentration or temporal reconfiguration of nodal roles. The next section investigates the latter by incorporating measured time-series data.
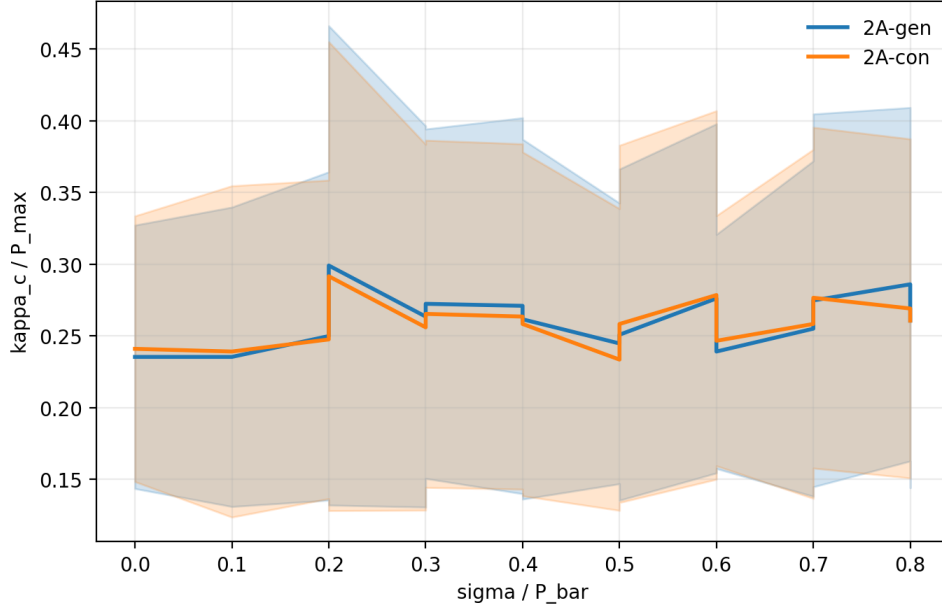
Figure 2: Effect of power magnitude heterogeneity on critical coupling. The horizontal axis shows relative dispersion $\sigma/\bar{P}$ for generator-side (blue) and consumer-side (red) perturbations, with the vertical axis showing $\bar{\kappa}_c/P_{\max}$.

2.5 Data-Driven Temporal Dynamics

The preceding analysis showed that static power distributions produce at most modest variations in κ_c. Real microgrids, however, do not operate at fixed configurations: household demand and photovoltaic generation fluctuate on diurnal and seasonal timescales, continuously reshaping the network's position on the configuration simplex. To capture these dynamics, the model is now driven by measured data.

A 49-household microgrid embedded in a $WS(n = 50, \bar{K} = 4, q = 0.1)$ topology is constructed, with one additional node serving as the point of common coupling (PCC). Household demand profiles are drawn from London smart-meter records [16], and photovoltaic generation profiles from UK Power Networks data [15]. The analysis focuses on a representative summer week (July) under a 100% PV scenario, defined as the stress-test limit in which every household is equipped with a PV installation sized to its annual demand, representing a worst-case surplus condition rather than a realistic deployment target. For each household i, the net power injection is

$$P_i(t) = g_i(t) - c_i(t), \tag{5}$$

where $g_i(t)$ denotes local PV generation and $c_i(t)$ represents demand. System-wide power balance is enforced through the PCC slack node:

$$P_{\mathrm{PCC}}(t) = -\sum_{i=1}^{49} P_i(t). \tag{6}$$

Each of the 336 half-hourly time steps (7 days $\times$ 48 intervals) is mapped onto the configuration simplex using ensemble averaging over 50 network realisations. The resulting trajectory, shown in fig. 4, reveals highly anisotropic daily motion. At night, most households are net consumers and the system resides in consumer-dominated simplex regions with $\eta_+ \approx 0.02$ and
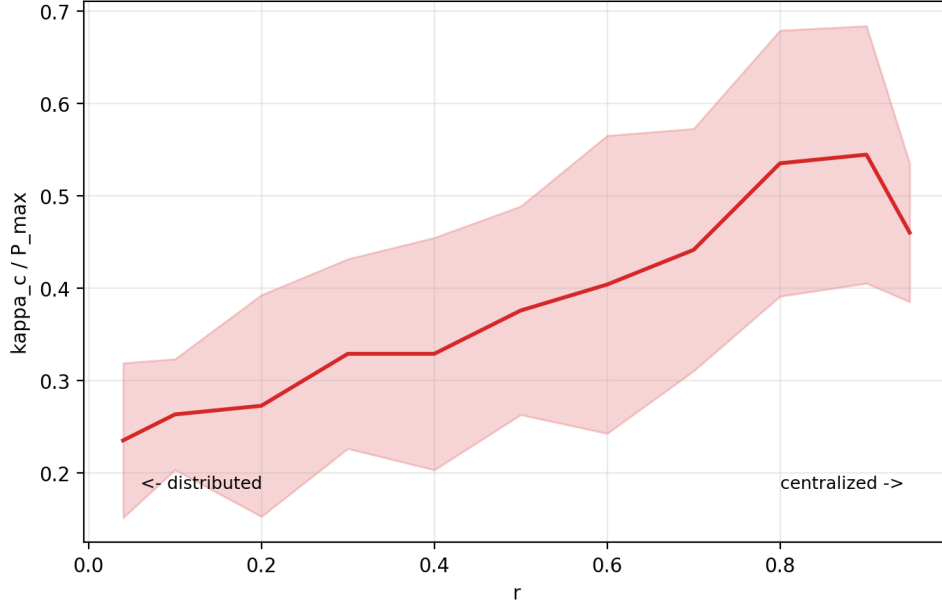
Figure 3: Effect of generation centralisation on critical coupling. The horizontal axis shows the centralisation ratio r (fraction of total generation carried by one node), with the vertical axis showing $\bar{\kappa}_c/P_{\max}$.

$\eta_- \in [0.15, 0.28]$. Around midday, strong PV output shifts a large fraction of nodes into net generation simultaneously, with η_+ peaking near 0.6 while η_- collapses toward zero. Rather than passing through the low-κ_c central regions, the trajectory remains confined to peripheral high-κ_c regions of the simplex.

This simplex motion translates into large, structured variation in critical coupling. Table 3 reports representative values from the weekly cycle, and fig. 5 shows the full time series.

Table 3: Critical coupling time series over a representative day, normalised by $P_{\max}$. The noon peak exceeds the dawn minimum by a factor of 22.6, far surpassing the 4% variation observed under static heterogeneity (section 2.4).

Time	$\kappa_c/P_{\max}$	σ	State
00:00	0.858	0.098	Night load
03:00	0.421	0.240	Pre-dawn
06:00	**0.294**	**0.003**	Dawn (most stable)
09:00	3.938	0.472	PV ramping
12:00	**6.653**	**0.650**	Noon (most vulnerable)
15:00	5.373	0.563	Afternoon
18:00	0.477	0.214	Evening
21:00	1.378	0.187	Night peak

The peak-to-valley ratio is

$$\frac{6.653}{0.294} = 22.6, \tag{7}$$

which far exceeds the 4% variation produced by static heterogeneity in section 2.4. This confirms that temporal dynamics, not static power distributions, are the dominant driver of synchronisation instability in data-driven microgrids. Notably, the most vulnerable state coincides
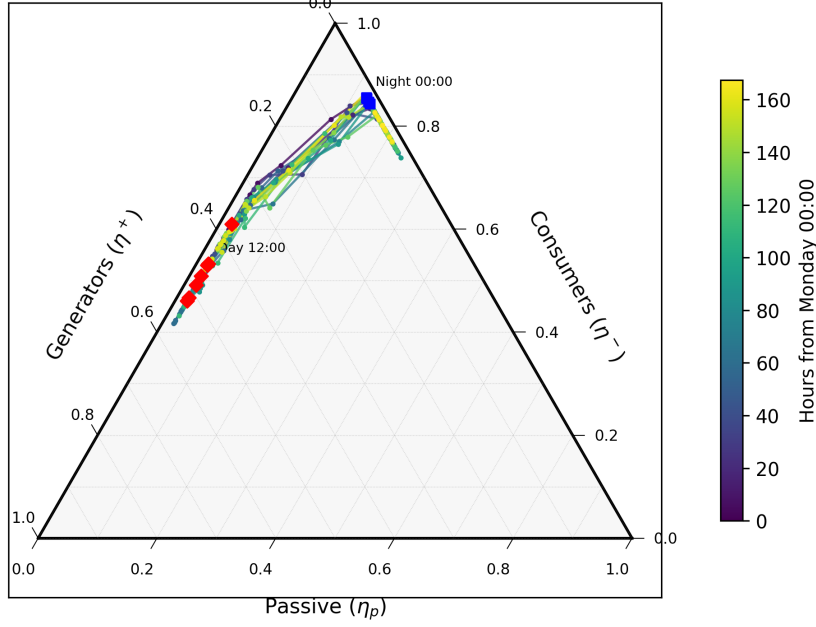
Figure 4: Configuration-simplex trajectory over one summer week under 100% PV balancing. Each point represents one half-hourly time step, coloured by time of day. The trajectory exhibits cyclic migration between night consumer-dominated states (lower right) and midday generator-dominated states (upper left), remaining near peripheral simplex regions associated with higher synchronisation fragility. The system avoids the low-κ_c central balanced region throughout the daily cycle.

with synchronised surplus generation at noon rather than with peak demand, indicating that instability arises from concentrated export pressure during PV maxima.

2.6 PCC Bottleneck Identification

The noon vulnerability peak identified in section 2.5 demands a mechanistic explanation. Around midday, nearly all 49 households become net generators, forcing the PCC to absorb the entire aggregate surplus. With $|P_{\mathrm{PCC}}| \approx 62$ kW flowing through $\deg(\mathrm{PCC}) = 4$ edges, the per-edge stress at the PCC is

$$\frac{|P_{\mathrm{PCC}}|}{\deg(\mathrm{PCC})} \approx \frac{62}{4} = 15.5 \text{ kW per edge.} \tag{8}$$

A typical household exports approximately 2 kW across four edges (≈ 0.5 kW per edge), so the PCC per-edge burden is roughly 30 times larger. Using the lower-bound intuition

$$\kappa_c \gtrsim \max_i \frac{|P_i|}{\deg(i)}, \tag{9}$$

the node with the largest stress-to-degree ratio dominates the synchronisation requirement—and in this system, that node is unambiguously the PCC.

This analysis establishes the central finding of the chapter: data-driven PV microgrids experience extreme noon instability, and the root cause is a topological bottleneck at the point of common coupling. The PCC must absorb the aggregate surplus of the entire microgrid through a small number of edges, creating a structural constraint that dwarfs all static distribution effects. This bottleneck is not a feature of the data or the particular household sample; it is a
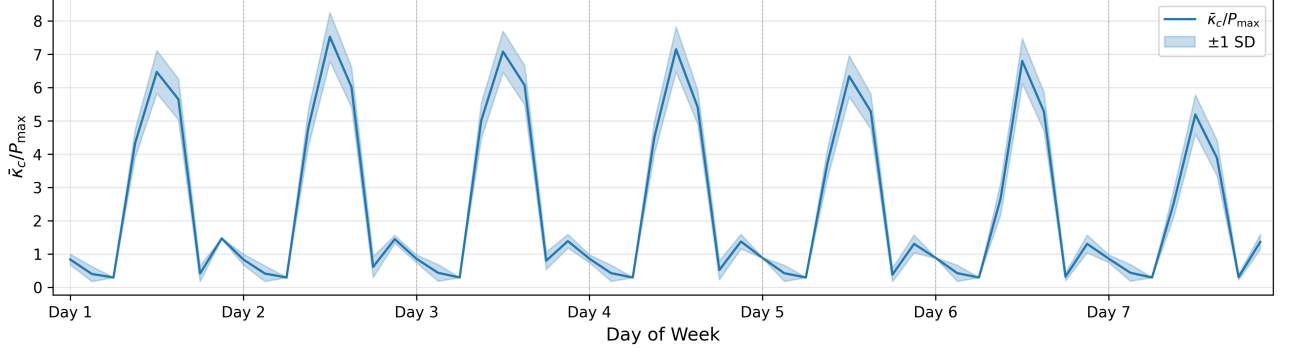
Figure 5: Weekly critical-coupling profile under summer operation. The vertical axis shows $\bar{\kappa}_c/P_{\max}$ (ensemble-averaged over 50 realisations), and the horizontal axis spans seven days at half-hourly resolution. A pronounced midday spike appears consistently each day, with a peak-to-valley ratio of 22.6 between the noon maximum ($\kappa_c/P_{\max} \approx 6.65$) and the dawn minimum ($\approx 0.29$). The most vulnerable state coincides with synchronised PV surplus, not with peak demand.

likely structural consequence of PCC-mediated microgrid architecture under synchronised renewable generation, at least for networks of this scale and topology. The identification of this local, degree-driven constraint motivates targeted structural intervention, which is the subject of section 3.

3   Topology Optimisation Method

Section 2 identified a structural bottleneck at the PCC as the root cause of noon synchronisation vulnerability. This chapter develops a targeted topology intervention to address it. The approach proceeds from physical motivation through analytical justification to method design and feasibility demonstration.

3.1   Motivation: Why Topology?

The PCC bottleneck identified in section 2.6 is a local, degree-driven constraint. A natural first question is whether *global* network restructuring can alleviate it. To test this, a sweep over rewiring probability $q \in \{0, 0.05, 0.1, 0.2, 0.4, 0.6, 0.8, 1.0\}$ was conducted on $WS(n = 50, \bar{K} = 4)$ networks, evaluating 50 ensembles across 56 timestamps (7 days $\times$ 8 representative hours) at each value of q.

The result, shown in fig. 6, is negative but informative. The noon critical coupling $\bar{\kappa}_c/P_{\max}$ remains between 6.6 and 6.7 across all q, varying by less than 1.5%. Despite substantial changes in global graph statistics—path length, clustering coefficient, degree of randomness—the synchronisation threshold is effectively unchanged. This confirms that the bottleneck is controlled by local node-level properties (the PCC stress-to-degree ratio) rather than by global network structure, and motivates targeted edge addition to the PCC specifically.
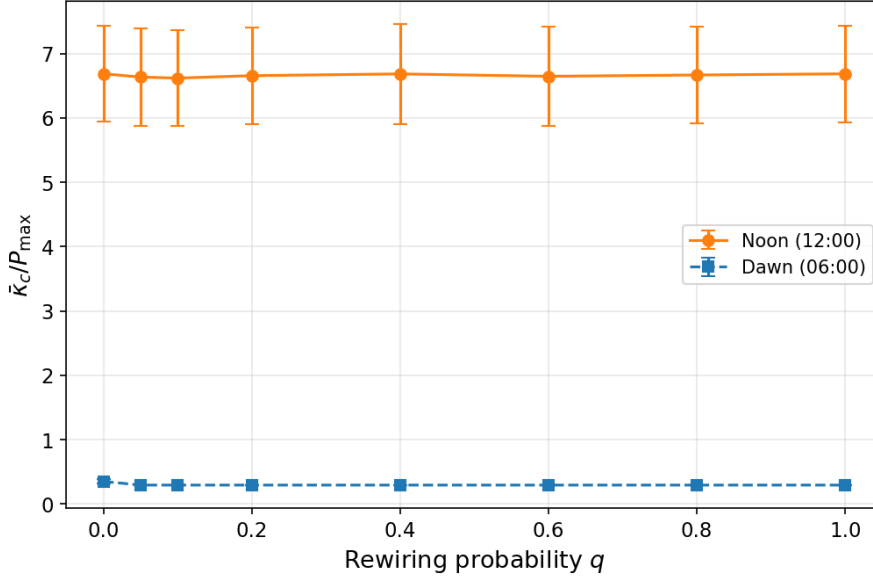
Figure 6: Critical coupling as a function of rewiring probability q. The noon threshold $\bar{\kappa}_c/P_{\max}$ (upper curve) remains between 6.6 and 6.7 across all q, and the dawn threshold (lower curve) clusters tightly around 0.294. Despite substantial changes in global network statistics (path length, clustering coefficient), neither the noon nor the dawn synchronisation threshold is materially affected. This confirms that the stability bottleneck is node-local rather than governed by global topology.

3.2 Analytical Foundation

The negative result of section 3.1 establishes that global topology is irrelevant to the PCC bottleneck. The natural follow-up question is *why* local degree augmentation should help. We address this in two steps: first a qualitative argument from the steady-state equations, then a formal lower bound on the critical coupling.

At a synchronised equilibrium the swing equation reduces to an implicit relationship between power injections, coupling strength, and phase differences:

$$P_i = \kappa \sum_{j \in \mathcal{N}(i)} \sin(\theta_i - \theta_j).$$

For fixed topology the phase differences $\theta_i - \theta_j$ are implicitly determined by κ and the power vector $\mathbf{P}$. Because sin is bounded by unity, each term on the right-hand side can contribute at most κ to balancing P_i. As $|P_i|$ grows or κ decreases toward its critical value κ_c, the steady-state phase differences are driven toward $\pm\pi/2$, beyond which the sinusoidal coupling can no longer maintain synchronisation.

In the residential network considered here, the PCC carries roughly 30 times the power of an individual household inverter, making it the first node whose phase differences approach the critical angle. Adding edges to the PCC increases $|\mathcal{N}(\text{PCC})|$, thereby distributing the synchronisation burden across more neighbours and pulling each individual phase difference back from $\pi/2$. This is the mechanism by which local degree augmentation lowers κ_c.

This intuition can be made more precise through the Jacobian structure of the steady-state map. Defining $F_i(\boldsymbol{\theta}, \kappa, \mathbf{P}) = P_i - \kappa \sum_{j \in \mathcal{N}(i)} \sin(\theta_i - \theta_j)$, the Jacobian of $\mathbf{F}$ with respect to $\boldsymbol{\theta}$ takes the form $J = -\kappa L_{\cos}$, where $L_{\cos}$ is a weighted graph Laplacian with edge weights $w_{ij} = \cos(\theta_i - \theta_j)$. When all phase differences satisfy $|\theta_i - \theta_j| < \pi/2$, every weight is positive

10

and $L_{\cos}$ is positive semi-definite with a one-dimensional null space spanned by the constant vector; restricted to the synchronisation subspace, J is negative definite. The implicit function theorem then guarantees that the equilibrium $\boldsymbol{\theta}^*(\kappa, \mathbf{P})$ varies smoothly with the parameters, and standard results in coupled-oscillator theory [5] establish that increasing $|P_i|$ monotonically increases the associated phase differences. The synchronised equilibrium ceases to exist precisely when some edge reaches $|\theta_i^* - \theta_j^*| = \pi/2$, at which point $\cos(\theta_i - \theta_j) = 0$, the Jacobian becomes singular, and the system undergoes a saddle-node bifurcation. Since the PCC carries the largest $|P_i|/\deg(i)$ ratio by a factor of approximately 30, it is the first node whose edges approach this critical angle.

The following theorem makes the intuition precise by providing a strict lower bound on the critical coupling in terms of PCC degree.

Theorem 3.1. *For any intervention that increases PCC degree to $d_0 + m$, the critical coupling satisfies*

$$\kappa_c \geq \frac{|P_{\mathrm{PCC}}|}{d_0 + m}. \tag{10}$$

Proof. At a synchronised steady state where $\ddot{\theta}_k = \dot{\theta}_k = 0$, section 2.1 reduces to

$$P_i = \kappa \sum_{j \in \mathcal{N}(i)} \sin(\theta_i - \theta_j). \tag{11}$$

Applying eq. (11) to the PCC at threshold $\kappa = \kappa_c$ and using $|\sin(x)| \leq 1$,

$$|P_{\mathrm{PCC}}| \leq \kappa_c(d_0 + m). \tag{12}$$

Rearranging gives eq. (10). $\square$

Dividing both sides of eq. (10) by $P_{\max}$ and defining the normalised threshold $\hat{\kappa}_c = \kappa_c/P_{\max}$, we obtain

$$\hat{\kappa}_c \geq \frac{|P_{\mathrm{PCC}}|}{P_{\max}(d_0 + m)}. \tag{13}$$

Under noon conditions, $|P_{\mathrm{PCC}}|/P_{\max} = 20.85$ and $d_0 = 4$, so eq. (13) becomes $\hat{\kappa}_c \geq 20.85/(4 + m)$. This bound establishes that increasing $\deg(\mathrm{PCC})$ is the theoretically grounded direction for reducing the critical coupling: each additional edge relaxes the constraint by distributing the synchronisation burden across more neighbours. The bound itself is elementary—it follows directly from $|\sin x| \leq 1$—and is not tight: numerical results in section 4.1 show that the empirical prefactor exceeds the theoretical one by 23–28%. Its value lies not in the constant but in establishing the correct *scaling*: κ_c decreases as $1/(d_0 + m)$, which the numerical experiments confirm with high fidelity.

3.3 Edge Addition Strategies

Recent work has shown that heterogeneous edge additions can improve synchronizability in oscillatory power networks [20]. Guided by theorem 3.1, three directed edge-addition strategies are defined, each motivated by a different physical heuristic:

(1) **Max Power.** Connect the node pairs with the highest sum of $|P_{\max}|$, targeting the largest stress contributors directly.

11

(2) **Score-based.** Rank candidate edges by $|P|/[d(d + 1)]$ with an opposite-sign constraint between endpoints, balancing stress relief against existing connectivity.

(3) **PCC Direct.** Connect the PCC to m randomly selected non-neighbours, providing the most direct degree augmentation.

A random baseline (uniformly sampling non-adjacent node pairs) is included for comparison. All strategies use the full-day maximum $|P_i|$ for edge selection, reflecting the fact that added edges represent permanent infrastructure.

3.4 Feasibility Demonstration ($m = 4$)

To demonstrate that targeted edge addition is effective, the three directed strategies and the random baseline were evaluated under a budget of $m = 4$ additional edges, with 50 ensemble realisations. Table 4 summarises the noon results.

Table 4: Strategy comparison at noon under a budget of $m = 4$ additional edges. All three directed strategies reduce the noon critical coupling by approximately 50%, while random addition provides only marginal improvement (3.4%).

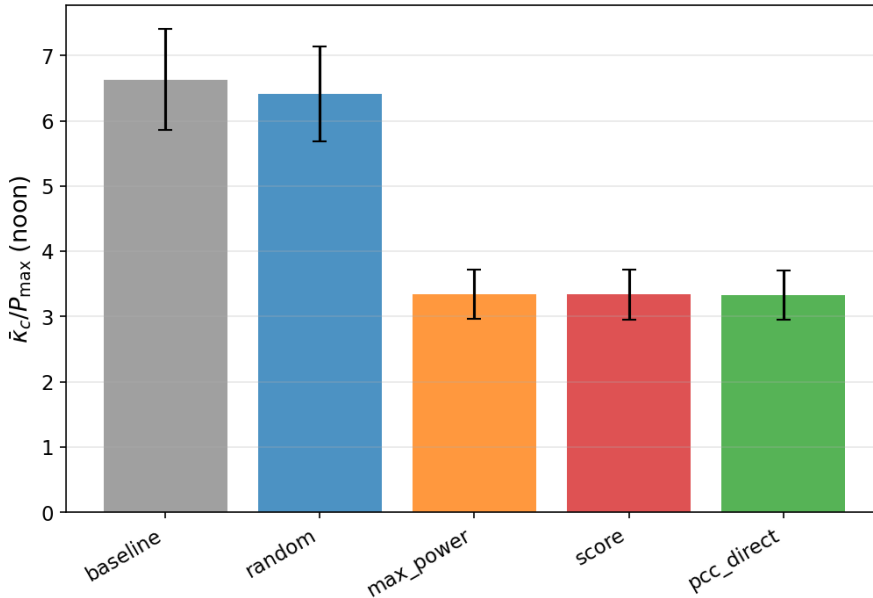| Strategy	$\bar{\kappa}_c(\text{Noon})/P_{\text{max}}$	Change
Baseline	6.634	—
Random	6.412	-3.4%
Max Power	3.346	-49.6%
Score	3.339	-49.7%
PCC Direct	3.331	-49.8%

Figure 7: Bar comparison of noon critical coupling across strategies for $m = 4$. The three directed strategies (Max Power, Score, PCC Direct) achieve nearly identical reductions of approximately 50%, while random edge addition barely improves upon the baseline. Error bars show one standard deviation across 50 ensemble realisations.
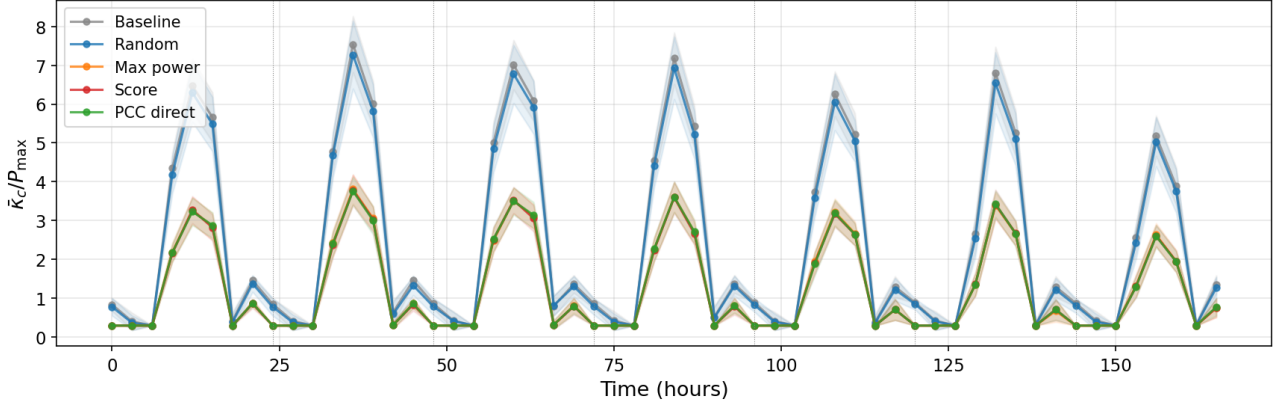
Figure 8: Seven-day $\kappa_c(t)$ trajectories for each strategy at $m = 4$. Directed strategies (coloured curves) remain consistently below the baseline and random curves throughout the daily cycle, preserving the temporal shape while uniformly compressing the amplitude. The three directed strategies are visually indistinguishable, confirming their functional equivalence.

All three directed strategies reduce $\bar{\kappa}_c(\text{Noon})$ by approximately 50%, while random addition achieves only 3.4% improvement (fig. 7). The differences among the three directed strategies are below 0.5%, making them practically equivalent. This near-equivalence is itself informative: although motivated by different heuristics, all three strategies ultimately place their added edges in the PCC neighbourhood, because the PCC dominance ($\sim 30\times$ stress ratio from section 2.6) overwhelms all other considerations. The seven-day time series in fig. 8 confirms that the reduction is consistent across the full diurnal cycle, with the temporal shape preserved but uniformly compressed.

These results establish that targeted PCC edge addition is a viable intervention. The next chapter scales this analysis systematically across edge budgets and validates the approach against an independent failure mode.

4 Numerical Experiments & Results

Section 3 demonstrated that $m = 4$ directed edges reduce the noon critical coupling by approximately 50%. This chapter scales the analysis to a systematic budget sweep, identifies the governing scaling law, and then tests whether the topology intervention transfers to cascade failure resilience—a mechanistically distinct failure mode.

4.1 Budget Scaling and Convergence

Building on the feasibility result of section 3.4, the edge budget was swept systematically over $m \in \{0, 1, 2, 4, 6, 8, 10, 15, 20\}$ with 50 ensemble realisations per strategy, consistent with the ensemble sizes used throughout this report. Figure 9 and table 5 present the results alongside the analytical lower bound from theorem 3.1.

Three conclusions emerge. First, the three directed strategies produce nearly identical results at every budget level, confirming that "add edges to PCC" matters far more than the particular

Table 5: Analytical lower bound versus observed noon critical coupling. The gap between the bound $20.85/(4 + m)$ and the observed κ_c/P_{max} remains in the range 23–28%, confirming that the bound captures the correct scaling while the constant offset reflects contributions from non-PCC nodes.

m	$d_0 + m$	Lower Bound	Observed κ_c/P_{max}	Gap
0	4	5.21	6.42	+23.2%
4	8	2.61	3.23	+23.8%
8	12	1.74	2.16	+24.2%
20	24	0.87	1.11	+28.1%

heuristic used. Second, the critical coupling follows inverse-degree scaling:

$$\frac{\kappa_c}{P_{max}} \approx \frac{25.7}{4 + m}, \tag{14}$$

with residuals below 5%, consistent with the analytical bound at a roughly 23% gap that reflects contributions from non-PCC nodes. Third, diminishing returns set in beyond $m \approx 10$: the budget $m = 4$ already yields 50% reduction, while $m = 20$ reaches 83%. The day–night variation is preserved but uniformly compressed at all budget levels.
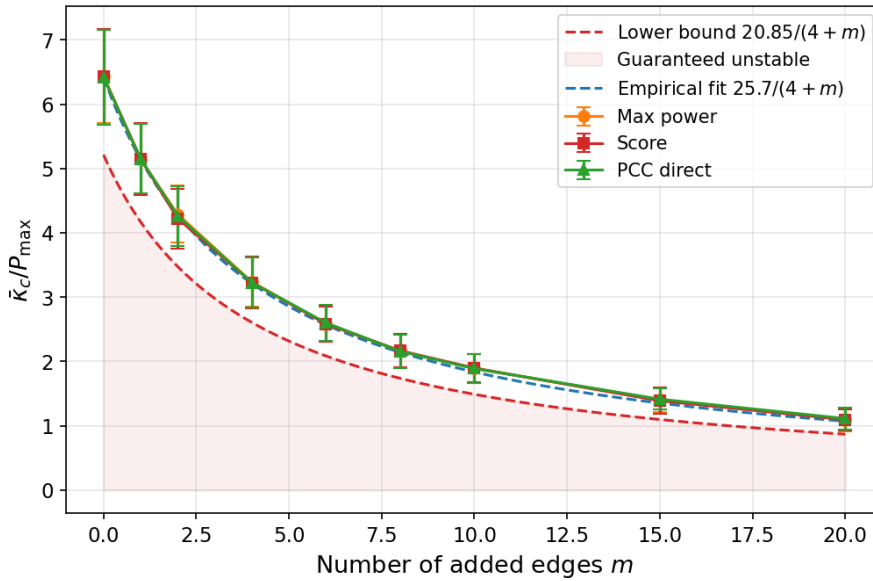

Figure 9: Budget sweep: normalised critical coupling κ_c/P_{max} as a function of added edges m. Directed-strategy data points (markers) nearly overlap at every budget level. The red dashed curve shows the analytical lower bound $20.85/(4 + m)$ from theorem 3.1; the blue dashed curve shows the empirical fit $25.7/(4 + m)$; the shaded region denotes guaranteed instability below the bound. The three directed strategies converge to a single inverse-degree scaling law, with $m = 4$ achieving 50% reduction and $m = 20$ reaching 83%.

The convergence of all strategies to a single scaling law is the key structural result of this section: in data-driven PCC microgrids of this scale and architecture, the optimisation landscape appears to have essentially one degree of freedom—PCC degree.

4.2 Cascade Failure Analysis

The preceding results concern synchronisation (swing-equation) stability. However, real grids also fail through overload-driven cascading failures—a mechanistically distinct process. Cascading failure models have been extensively studied in network science [17, 2, 9], including dynamically induced cascading failures specific to power grids [12]. To test whether the topology intervention transfers to this second failure mode, the DC cascade model of Smith et al. [14] is adopted. The linearised DC power flow gives phase angles $\boldsymbol{\theta} = L^\dagger \boldsymbol{P}$ (where $L^\dagger$ is the graph-Laplacian pseudo-inverse) and edge flows

$$f_{kl} = B_{kl}(\theta_k - \theta_l), \tag{15}$$

with susceptance $B_{kl} = 1$. The cascade proceeds iteratively: all edges with $|f_e| > \alpha$ are tripped, flows are recomputed in each connected component, and the process repeats until no further trips occur. The survival ratio $S = |\text{surviving edges}|/|\text{initial edges}|$ quantifies resilience.

Baseline validation without added edges confirms the cascade model responds meaningfully to network parameters: at $n = 50$, survival curves display a sharp sigmoidal crossover near $\alpha/\alpha^* \approx 1$ with low ensemble variance, whereas $n = 10$ networks show gradual transitions with high variability. More structured topologies (lower q) exhibit higher survival in the low-tolerance regime. These controls ensure that any absence of improvement under PCC edge addition cannot be attributed to insensitivity of the cascade framework.

The experiment uses 50 ensemble realisations across 5 time slices (00:00, 06:00, 09:00, 12:00, 18:00) and 4 topologies ($m = 0$, $m = 4$ PCC direct, $m = 4$ random, $m = 8$ PCC direct), with 50 tolerance values α/α^* in $[0.1, 2.5]$, where $\alpha^* = f_{\max}$ is the initial maximum edge current for each configuration.

Figure 10 presents the central negative result. In stark contrast to the swing-stability findings, adding edges to the PCC does not improve cascade resilience and often worsens it: the $m = 8$ PCC direct configuration is consistently the weakest across all time slices. Random edge addition is nearly indistinguishable from the baseline.

The mechanism is revealed by fig. 11: PCC edges carry approximately $11\times$ the network-average current and fail first in all configurations. Additional PCC edges do not prevent the cascade; they merely redistribute the overload among more PCC-adjacent edges, all of which remain far above the network mean and trip in sequence.

To verify that this step-like survival pattern is a structural consequence of PCC heterogeneity rather than a numerical artefact, a control experiment was conducted on 100 uniform (no-PCC) $WS(50, 4, 0.1)$ networks with $P = \pm 1/25$.

As shown in fig. 12, the control recovers the smooth sigmoid cascade curve reported by Smith et al. [14], confirming that PCC structural heterogeneity—not numerics—is responsible for the step-like behaviour. A complementary view of cascade dynamics comes from the recursion depth: whereas fig. 10 shows the final survival outcome, fig. 13 tracks how many redistribution–trip rounds the cascade takes to reach that outcome.

The $m = 8$ PCC direct configuration reaches the largest cascade depth (peak $T \approx 3.5$ rounds), meaning additional PCC edges stretch the failure process over more rounds without preventing the outcome. Baseline and random configurations remain closer to one-shot PCC isolation, consistent with their higher survival ratios.
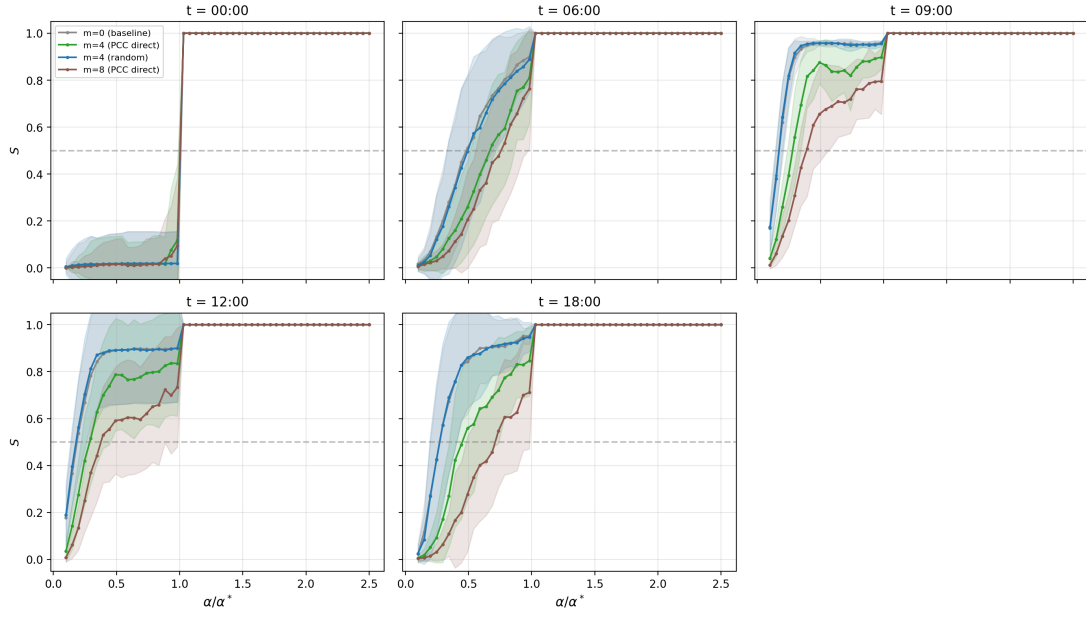
Figure 10: Cascade survival ratio S versus normalised tolerance α/α^* across five time slices and four topologies. Adding PCC-directed edges does not improve cascade resilience: the $m = 8$ PCC direct configuration (red) is consistently the weakest across all time slices. Random addition is nearly indistinguishable from the baseline. The step-like curve shape (rather than a smooth sigmoid) is a physical consequence of PCC structural heterogeneity, as confirmed by the control experiment in fig. 12.

The mechanism is consistent across all diagnostics: PCC edges carry the highest currents and trip first; power redistributes to remaining PCC edges, triggering further overloads; repeated rounds eventually isolate the PCC. Final survivability depends on whether internal subnetworks can self-supply after PCC isolation, not on whether PCC degree was increased.
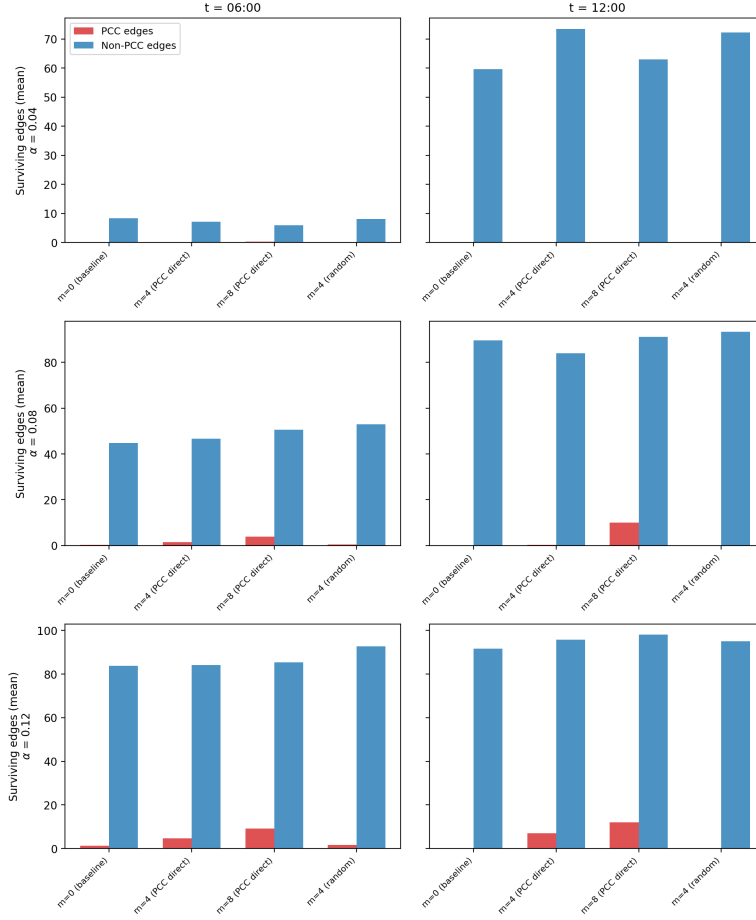
16

Figure 11: Edge survival analysis at fixed absolute tolerance slices. Red bars indicate PCC edges; blue bars indicate non-PCC edges. PCC edges carry approximately $11\times$ the mean network current at noon and fail first in all configurations, acting as the initial domino in every cascade. Even when $m = 8$ partially spreads flow across more PCC edges, the total survival ratio does not improve because final outcomes depend on whether isolated subnetworks can self-supply after PCC disconnection.
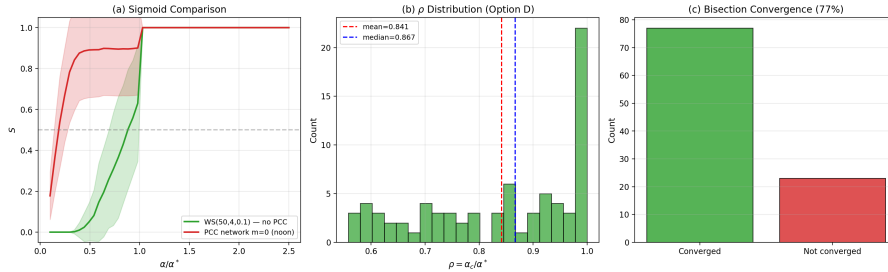

Figure 12: Control experiment: cascade behaviour in 100 uniform (no-PCC) $WS(50, 4, 0.1)$ networks with $P = \pm 1/25$. The control recovers smooth sigmoid behaviour consistent with Smith et al. [14], confirming that the step-like pattern observed in PCC networks is a physical consequence of structural heterogeneity, not a numerical artefact.
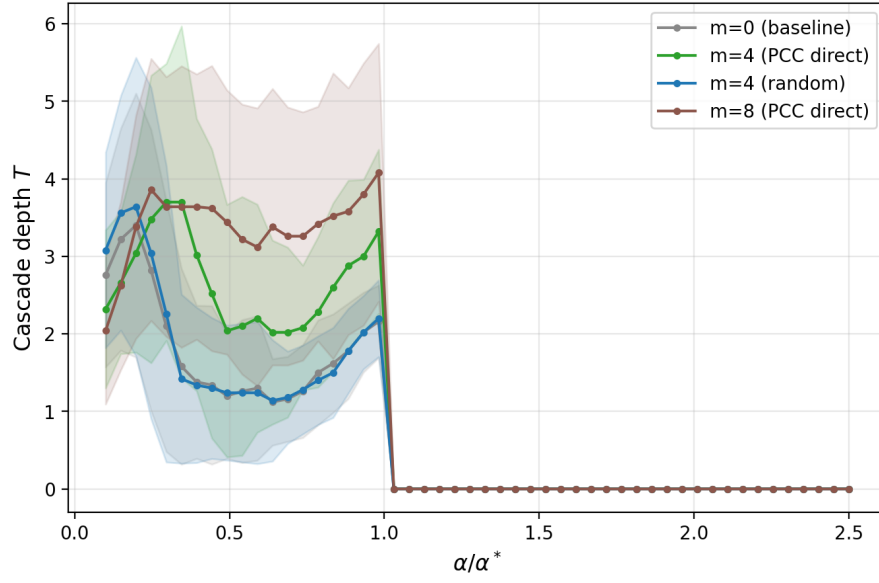
Figure 13: Cascade recursion depth T versus normalised tolerance α/α^* at noon. The $m = 8$ PCC direct configuration reaches the largest cascade depth (peak $T \approx 3.5$ rounds), indicating that additional PCC edges stretch the failure process over more redistribution–trip rounds without preventing the eventual outcome. Baseline and random configurations remain closer to one-shot PCC isolation.

4.3 Sensitivity Analysis: Damping Parameter Sweep

The preceding sections established the topology intervention and identified its contrasting effects on synchronisation and cascade resilience. All results thus far used a damping coefficient $\gamma = 1$. Since increasing renewable penetration reduces effective system inertia (equivalent to lower γ), it is important to verify that the topology optimisation benefit is not an artefact of a particular damping regime.

A sweep over $\gamma \in [0.1, 5.0]$ (16 values) was conducted with 50 ensemble realisations at a Wednesday noon time slice, comparing the baseline ($m = 0$) against PCC direct with $m = 4$. Because the sweep uses a single noon snapshot rather than the seven-day noon average employed in section 3, absolute κ_c values are approximately 12% higher than the weekly averages reported earlier; the relative comparisons between $m = 0$ and $m = 4$ presented in the preceding sections are unaffected.

Table 6: Damping sensitivity: critical coupling at noon for baseline ($m = 0$) and PCC direct ($m = 4$) at five representative damping values. The relative reduction remains within 49–50% across the full range, while the absolute improvement $\Delta\kappa_c$ is largest at low γ.

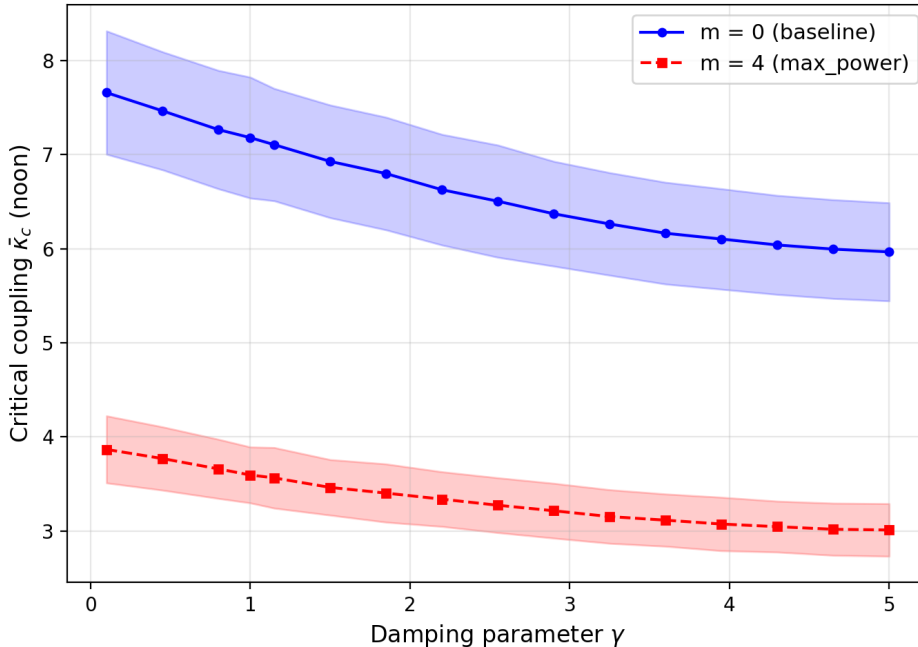| γ	κ_c ($m = 0$)	κ_c ($m = 4$)	$\Delta\kappa_c$	Relative
0.10	7.66 ± 0.66	3.87 ± 0.36	3.79	-49.5%
1.00	7.18 ± 0.64	3.60 ± 0.30	3.59	-49.9%
2.20	6.63 ± 0.59	3.34 ± 0.29	3.29	-49.6%
3.60	6.16 ± 0.54	3.12 ± 0.28	3.05	-49.5%
5.00	5.97 ± 0.52	3.01 ± 0.28	2.96	-49.5%

Figure 14: Damping sensitivity: κ_c at noon as a function of γ for baseline ($m = 0$, upper curve) and PCC direct ($m = 4$, lower curve). Both curves decrease monotonically with γ, and the vertical gap between them narrows in absolute terms while the relative reduction remains constant at approximately 50%. Error bands show one standard deviation across 50 ensemble realisations.

Three findings emerge from table 6 and fig. 14. First, κ_c decreases monotonically with γ for both the baseline and augmented topologies, as expected from the stabilising role of the damping term in section 2.1. Second, the relative reduction in κ_c achieved by the $m = 4$ intervention remains within 49–50% across all values of γ, indicating that the topology benefit is effectively damping-invariant. Third, the absolute improvement $\Delta\kappa_c$ decreases from 3.79 at $\gamma = 0.1$ to 2.96 at $\gamma = 5.0$, meaning the intervention provides the greatest absolute benefit precisely where it is most needed—in low-inertia systems characteristic of high-renewable penetration.

These results confirm that the topology optimisation findings of section 3 are robust to damping variation and are not contingent on the particular value $\gamma = 1$.

5 Discussion & Conclusion

5.1 Synthesis

The findings form a coherent causal chain, summarised in table 7. Static power heterogeneity proved negligible as an instability driver, while measured diurnal data revealed a 22.6-fold day–night swing in critical coupling whose root cause was unambiguously localised to the PCC. Targeted degree augmentation resolved that vulnerability under swing-equation dynamics, following an inverse-degree scaling law analytically grounded in theorem 3.1, yet the same structural change offered no benefit—and often caused harm—under cascade failure, a mechanistically independent failure mode whose robustness to damping variation was confirmed across $\gamma \in [0.1, 5.0]$.

Table 7: Integrated findings across the analysis. Each row identifies a core result and its narrative role in the causal chain.

Chapter	Core Finding	Narrative Role
Ch. 2 (Static)	4% variation under heterogeneity; 139% under centralisation	Rules out static variance; shifts attention to dynamics and concentration
Ch. 2 (Temporal)	22.6× day–night κ_c swing; PCC bottleneck	Identifies the structural root cause of noon vulnerability
Ch. 3–4 (Topology)	Directed PCC edges reduce κ_c by 50–83%; $1/(d_0 + m)$ scaling	Provides actionable intervention with interpretable scaling
Ch. 4 (Cascade)	Same intervention degrades cascade resilience	Cross-validates under second failure mode; reveals paradox
Ch. 4 (Sensitivity)	Relative reduction ∼50% across all γ	Confirms robustness to damping variation

5.2 The Stability–Resilience Paradox

The contrast between the synchronisation and cascade results constitutes the central paradox of this work. Table 8 summarises the opposing effects.

Table 8: Opposite effects of the same topology intervention under two failure modes. Adding PCC edges is beneficial for swing stability but neutral or harmful for cascade resilience, owing to mechanistically independent response channels.

Failure Dimension	Effect of Adding PCC Edges	Dominant Mechanism
Swing Stability	Beneficial (lower κ_c)	Synchronisation burden distributed across more PCC neighbours
Cascade Resilience	Neutral/harmful (no gain in S)	Current concentrates on PCC edges; amplifies overload propagation

This outcome echoes the classic Braess paradox, which has been identified in oscillator networks [19] and characterised through linear stability analysis [3]. There, adding a link to a network can reduce stability within the same dynamical model—the intervention undermines the very objective it targets. What we observe here is structurally similar but cuts across models rather than within one: PCC edge addition is beneficial under swing-equation synchronisation and neutral or harmful under DC cascade dynamics. In the classical Braess setting, the comparison is between pre- and post-expansion states within a single objective landscape. Here, the same topological change crosses objective landscapes entirely, reversing sign between them. A security gain demonstrated under one failure model therefore carries no guarantee of transfer to another.

For grid planners, the implication is uncomfortable but clear. A topology that looks robust under synchronisation analysis may be quietly fragile to overload-triggered cascades. Evaluating these two failure modes separately—and optimising for only one—risks a false sense of security. Resilience assessment should treat synchronisation thresholds and cascade outcomes as joint constraints, not competing alternatives.

5.3   Limitations and Future Directions

Several modelling choices bound the scope of these conclusions. Homogeneous coupling, uniform damping, and a linearised DC cascade approximation are adopted throughout; a full AC treatment with heterogeneous line impedances would introduce additional degrees of freedom and may alter the quantitative balance between failure modes. The analysis is restricted to $n = 50$ nodes under a single summer week of data, leaving open questions about scaling to larger networks and about seasonal variability, particularly under low-irradiance winter conditions.

For practitioners, PCC degree augmentation is a viable and cost-effective tool for reducing synchronisation vulnerability, but it must be paired with complementary cascade-mitigation mechanisms—dynamic line rating, controlled islanding, and layered protection settings—rather than treated as a self-sufficient intervention. Future work should examine multi-PCC configurations and interconnected microgrid clusters, pursue joint optimisation of storage dispatch and network topology under dual synchronisation–cascade objectives, and test the inverse-degree scaling law against stochastic weather and load ensembles at distribution-planning scales.

References

[1] Piotr Bojek. *Renewables - energy system - IEA*. Jan. 2026. URL: https://www.iea.org/energy-system/renewables.

[2] Benjamin A Carreras et al. "Critical points and transitions in an electric power transmission model for cascading failure blackouts". In: *Chaos: An interdisciplinary journal of nonlinear science* 12.4 (2002), pp. 985–994.

[3] Tommaso Coletta and Philippe Jacquod. "Linear stability and the Braess paradox in coupled-oscillator networks and electric power grids". In: *Physical Review E* 93.3 (2016), p. 032222.

[4] Department for Energy Security and Net Zero. *Digest of UK Energy Statistics 2025: Chapters 1–7*. Statistical Report. Department for Energy Security and Net Zero, 2025. URL: https://assets.publishing.service.gov.uk/media/68dbe477ef1c2f72bc1e4c4d/DUKES_2025_Chapters_1-7.pdf.

[5] Florian Dörfler and Francesco Bullo. "Synchronization in complex networks of phase oscillators: A survey". In: *Automatica* 50.6 (2014), pp. 1539–1564. DOI: 10.1016/j.automatica.2014.04.012.

[6] Insight Distributed Energy. *Microgrid vs Traditional Grid*. Jan. 2025. URL: https://insightdistributedenergy.com/blog/microgrid-solutions/microgrid-vs-traditional-grid/ (visited on 02/18/2026).

[7] Giovanni Filatrella, Arne Hejde Nielsen, and Niels Falsig Pedersen. "Analysis of a power grid using a Kuramoto-like model". In: *The European Physical Journal B* 61.4 (2008), pp. 485–491.

[8] Debsankha Manik et al. "Supply networks: Instabilities without overload". In: *The European Physical Journal Special Topics* 223.12 (2014), pp. 2527–2547.

[9] Adilson E Motter and Ying-Cheng Lai. "Cascade-based attacks on complex networks". In: *Physical review E* 66.6 (2002), p. 065102.

[10] Takashi Nishikawa and Adilson E Motter. "Comparative analysis of existing models for power-grid synchronization". In: *New Journal of Physics* 17.1 (2015), p. 015012.

[11] Martin Rohden et al. "Self-organized synchronization in decentralized power grids". In: *Physical review letters* 109.6 (2012), p. 064101.

[12] Benjamin Schäfer et al. "Dynamically induced cascading failures in power grids". In: *Nature communications* 9.1 (2018), p. 1975.

[13] Per Sebastian Skardal, Dane Taylor, and Jie Sun. "Synchrony-optimized networks of Kuramoto oscillators with inertia". In: *Physica A: Statistical Mechanics and its Applications* 460 (2016), pp. 146–156. DOI: 10.1016/j.physa.2016.07.009.

[14] Oliver Smith et al. "The effect of renewable energy incorporation on power grid stability and resilience". In: *Science advances* 8.9 (2022), eabj6734. DOI: 10.1126/sciadv.abj6734. eprint: https://www.science.org/doi/pdf/10.1126/sciadv.abj6734. URL: https://www.science.org/doi/abs/10.1126/sciadv.abj6734.

[15] U.K. Power Networks. *Photovoltaic (PV) Solar Panel Energy Generation Data*. Accessed: 2026-02-18. URL: https://data.london.gov.uk/dataset/photovoltaic-pv-solar-panel-energy-generation-data-2nlqm.

[16] U.K. Power Networks. *Smart Meter Energy Consumption Data in London Households*. Accessed: 2026-02-18. URL: https://data.london.gov.uk/dataset/smartmeter-energy-consumption-data-in-london-households-vqm0d.

[17] Duncan J. Watts. "A simple model of global cascades on random networks". In: *Proceedings of the National Academy of Sciences* 99.9 (2002), pp. 5766–5771. DOI: 10.1073/pnas.082090499. eprint: https://www.pnas.org/doi/pdf/10.1073/pnas.082090499. URL: https://www.pnas.org/doi/abs/10.1073/pnas.082090499.

[18] Duncan J. Watts and Steven H. Strogatz. "Collective dynamics of 'small-world' networks". In: *Nature* 393.6684 (1998), pp. 440–442. DOI: 10.1038/30918.

[19] Dirk Witthaut and Marc Timme. "Braess's paradox in oscillator networks, desynchronization and power outage". In: *New journal of physics* 14.8 (2012), p. 083036.

[20] Xian-Bin Zhang, Zhao-Yang Lu, and Zong-Hua Liu. "Influence of edge additions on the synchronizability of oscillatory power networks". In: *Communications in Nonlinear Science and Numerical Simulation* 41 (2016), pp. 1–10. DOI: 10.1016/j.cnsns.2016.04.030.